Atmos. Chem. Phys. Discuss., 6, 1509–1537, 2006
www.atmos-chem-phys-discuss.net/6/1509/2006/

Atmospheric Chemistry and Physics Discussions

Some ice nucleation characteristics of Asian and Saharan desert dust

P. R. Field[1,5], **O. Möhler**[2], **P. Connolly**[3], **M. Krämer**[4], **R. Cotton**[1], **A. J. Heymsfield**[5], **H. Saathoff**[2], **and M. Schnaiter**[2]

[1]Met Office, OBR (Observations Based Research), UK
[2]Forschungszentrum Karlsruhe, Institute for Meteorology and Climate Research (IMK-AAF), Germany
[3]University of Manchester, School of Earth, Atmospheric and Environmental Sciences, UK
[4]Forschungszentrum Jülich, Institute of Chemistry and Dynamics of the Geosphere (ICG-I), Germany
[5]NCAR, MMM (Mesoscale and Microscale Meteorology), USA

Received: 5 December 2005 – Accepted: 20 December 2005 – Published: 23 February 2006

Correspondence to: P. R. Field (prfield@ucar.edu)

Abstract

The large (7 m×4 m cylinder) AIDA (Aerosol Interactions and Dynamics in the Atmosphere) cloud chamber facility at Forschungszentrum, Karlsruhe, Germany was used to test the ice nucleating ability of two desert dust samples from the Sahara and Asia. At temperatures warmer than −40°C droplets were formed before ice crystals formed, there was no deposition nucleation observed. At temperatures colder than −40°C both dust samples exhibited dual nucleation events that were observed during the same expansion experiment. The primary nucleation event occurred at ice saturation ratios of 1.1 to 1.3 and is likely to be a deposition nucleation mode. The secondary nucleation event occurred at ice saturation ratios between 1.35 and 1.5. It is unclear whether this ice nucleation event is via a further deposition mode or a condensation mode. The activated fractions of desert dust ranged from ∼5–10% at −20°C to 20–40% at temperatures colder than −40°C. There was no obvious difference between the nucleation behaviour of the two dust samples.

1 Introduction

The role of desert dust in ice nucleation has recently been characterized in the Caribbean during the CRYSTAL-FACE (Cirrus Regional Study of Tropical Anvils and Cirrus Layers – Florida Area Cirrus Experiment) campaign when Saharan dust advected across the Atlantic into the field area (Sassen et al., 2003; DeMott et al., 2003; Cziczo et al., 2004). Desert dust is known to act as good deposition nuclei (e.g. Isono, 1953; Roberts and Hallett, 1968) but other nucleating properties associated with desert dust are not well characterized. If desertification continues to increase then the role of dust on ice microphysics will gain in importance and will need to be explicitly accounted for in weather and climate models. As computer models become more sophisticated they will include global sources and sinks of different aerosol species and will therefore be able to investigate the effects and importance of deposition ice nucleation on large

ACPD
6, 1509–1537, 2006

scale cloud systems.

DeMott et al. (2003) reported on ice nuclei measurements in a Saharan dust plume observed during the CRYSTAL-FACE experiment (Jensen et al., 2004). They found that at −36.5°C and a supersaturation with respect to ice of 23% they observed ∼1 cm^{-3} ice nuclei concentrations. These conditions are below water saturation so these observations represent the concentration of deposition nuclei. Coincident aerosol concentrations for sizes greater than 0.5 μm were ∼10 cm^{-3}. It is likely that the concentrations were higher, but even assuming background aerosol concentrations of 10 cm^{-3} gives an upper limit for ice nucleation efficiency of 0.1. During the same campaign Sassen et al. (2003) presented evidence suggesting that altocumulus clouds (−5 to −8°C) were being glaciated through interaction with the Saharan dust and Cziczo et al. (2004) showed that mineral dust was the dominant residue during the event found after in-situ ice particles were captured and evapourated. Analysis of CVI residuals (Targino et al., 2005) from the INTACC experiment (Field et al., 2001) showed that mineral dust is more prevalent in the cases where heterogeneous ice nucleation was observed to be active.

Recently, Zuberi et al. (2002) looked at the formation of ice on aqueous droplets ($(NH_4)_2SO_4$-H_2O, 10–50 μm in size) containing dust particles. They found that for significant mass fractions of dust (>27%) that the droplets froze at much lower saturations than would be expected for homogeneous freezing of a droplet without any dust inclusion. Similarly, Hung et al. (2003) showed that mineral dust inclusions increased the temperature at which ice nucleation occurs.

Previous laboratory work on the ice nucleating ability of kaolinite has been carried out by Roberts and Hallett (1968). They found that for freshly prepared samples that supersaturations with respect to ice of 20% at temperatures colder than −18°C were required for the kaolinite to act as an ice nuclei. Following the formation of ice they raised the temperature slightly to drive off the ice and repeated the experiment. They found that kaolinite particles that had previously formed ice crystals now activated at 10% supersaturation with respect to ice.

These results suggest that the role of desert dust in the evolution of clouds and precipitation may be important and provided motivation for the present study reported here and in a companion paper (Möhler et al., 2005). In this paper we report on a series of laboratory experiments carried out at the AIDA cloud and aerosol chamber facility in which two desert dust samples were tested under realistic atmospheric conditions and in relatively large numbers. In Sect. 2 the basic experimental procedure is outlined. In Sect. 3 the dust samples are described. In Sect. 4 the instrumentation used is described. Section 5 is a presentation of the results and Sects. 6 and 7, respectively, contain the discussion and conclusions.

2 Experimental procedure

The cylindrical AIDA aerosol vessel is 7m high and 4m in diameter. The aerosol vessel is located within a larger chamber that acts as a thermal buffer and provides control of the initial temperature within the aerosol vessel. A fan within the aerosol vessel ensures well mixed conditions with sample temperatures within the volume agreeing to ±0.3 K.

Ice nucleation experiments are started just below ice saturation inside the aerosol chamber. This is achieved by cooling the chamber to 273 K, evacuating the vessel to 0.01 mb, flushing twice with synthetic air, adding water vapour and filling the vessel to atmospheric pressure with synthetic air. Finally, the vessel is cooled to the starting temperature of the experiment.

To simulate the adiabatic cooling of rising air parcels the pressure within the chamber is reduced with a rate controllable mechanical pump from 1000 hPa to 800 hPa over typical pumping periods of 5 min. Mean cooling rates (close to the time of nucleation) for the experiments presented here were typically 1–2 K min^{-1} that is equivalent to ascent speeds of 1–3 m s^{-1}. The cooling in the aerosol vessel is not purely adiabatic: the aerosol vessel wall temperatures remain approximately constant throughout the expansion and as a consequence there is a heat flux from the vessel wall into the

chamber. Similarly, during the cooling the vapour pressure above the ice on the wall is greater than the vapour pressure in the chamber and a vapour flux into the chamber also occurs.

Before the candidate aerosol is added to the chamber a control run is made with the background conditions in the chamber. Once complete the candidate aerosol is added and then characterized with standard aerosol sampling intrumentation. Several expansions are carried out on the same candidate aerosol sample at different pump speeds (cooling rates) throughout the course of a day. Typically, during each series of 3 or 4 expansions, the first expansion was done at a higher cooling rate than the subsequent expansions. More details about the AIDA chamber and the experimental procedures can be found in Möhler et al. (2003, 2005).

3 Dust samples

Two surface samples of desert dust obtained from Asia (AD1) and the Sahara (SD2) were used. X-ray fluorescence analysis indicated that the Asian and Saharan dust samples were rich in silicon and calcium oxides, respectively. Möhler et al. (2005) gives more information concerning the results of X-ray analysis and aerosol distributions. The samples were dry re-dispersed producing aerosol distributions with a size range between 0.1 and 2 μm with mode diameters between 0.3 and 0.5 μm. Prior to the experiment the samples were stored in clean conditions and did not undergo any heating or crushing.

4 Instrumentation

The AIDA chamber is populated with many instruments (see Möhler et al., 2003, 2005), but we will briefly describe only the instrumentation referred to in this paper.

The temperature of the gas and wall of the chamber is measured at multiple locations with platinum resistance thermometers and thermocouples. These values are

combined and an average gas temperature accurate to ±0.3 K is computed. Pressure is measured with high precision Baratron sensors (MKS, Munich). An in situ multi-reflection path tunable diode laser absorption spectrometer directly measures the the water vapour concentration in the chamber volume. The TDL water vapour concentration is scaled to match a cryogenically cooled mirror hygrometer (LX373, MBW,Switzerland) that is accurate to better than ±0.1 K during the expansion phase before any condensate appears. The estimated error in the TDL water vapour concentration is ±5%. This device is located two thirds of the way up the chamber. The sample air for the humidity sensors is obtained through a 8 mm diameter inlet heated to 30°C located near the top of the chamber. Once particles are produced they will be ingested and evapourated as they enter the humidity measurement system. This effect results in the humidity measurement containing some contribution from the condensed water content. As the particles grow larger their collection efficiency by the humidity system decreases and the contribution from particles is difficult to quantify. Hence when condensed water contents are high the total water measurement can become unreliable. Combining the uncertainties in the temperature and water vapour concentration provides an estimate of the uncertainty in the 1-s humidity measurement of ±6% for the temperature and humidity range considered here.

Particles are detected and measured with the Small Ice Detector (SID) and Cloud Particle Imager (CPI: Stratton Park Engineering Company, SPEC Inc). These two probes were primarily designed to sample particles from aircraft, but can be used in the laboratory. Aerosol particles in the size range 0.01 to 10 μm are measured with a combination of a scanning mobility particle sizer (SMPS, TSI), an aerodynamic particle spectrometer (APS, TSI) and a CPC3010 (TSI) optical particle counter. In some cases the aerosol data was not available and so we made use of the Welas probe (Palas Aerosol Technology, Germany).

The hypothesis that liquid droplets are spherical and ice crystals are not spherical is the basis of the phase determination method used by the SID probe. The SID is a laser scattering device that can count and size spherical particles between 1 and 35 μm

(diameter) and count non-spherical particles. The probe uses six detectors arranged azimuthally at a forward scattering angle of 30°, with a seventh detector mounted at the forward scattering angle. One of the six 30° detectors has an iris fitted to allow it to define a 400×800 μm ellipse on the scattering laser. When light was detected by this detector and one other detector, a particle was known to be in the sample volume and the detector responses were recorded. By comparing the responses of the azimuthally arranged detectors an "asphericity factor" (Af) could be obtained for each particle measured that ranges from 0 for spherical particles to 100 for very non-spherical particles (see Hirst et al., 2001, for more details). The five 30° detectors that were not stopped down with the iris were used to compute Af using:

$$Af = k \frac{\sqrt{\sum_{i=1}^{5} (< E > - E_i)^2}}{< E >}, \quad (1)$$

where k is a constant (=22.361) set to place Af in the range 0–100, E_i are the detector values and $<E>$ is the mean of E_i. In practice, noise and differences between the detectors mean that the spherical droplets that should give Af=0 will in general produce non-zero values. Single particles must therefore be differentiated from ice by using a threshold value for the asphericity. Using a threshold can lead to some non-spherical particles being classed as spherical and vice-versa (see Field et al., 2004). The SID probe sampled from the chamber with a flow speed of ~5 m s^{-1} (~1 cm^3 sampled per second). This flow speed is very different from aircraft speeds so the instrument used different calibration constants for sizing. Particle sizing from this instrument assumes that the particle is spherical. Therefore, non-spherical particles will be incorrectly sized, but this "spherical size" can still be used qualitatively to assess if ice particles are growing.

The CPI is a 2-D imaging probe designed to take high resolution images of cloud ice crystals and large droplets. It has two particle detection lasers which intercept at the probes sample area (located within the probes air sampling tube at the focal plane of an objective lens; the images are magnified using a galilean telescope arrangement)

and fall onto a photomultiplier dump spot. Once particles are detected with the particle detection lasers/photomultipliers a high power, 20 ns pulsed laser is armed which is directed through the sample area, falling onto a charge coupled device (CCD) camera, which consequently images the shadow of the particle. Since the distance of the particle from the object plane is comparable to the size of the particle, the images are well described by the Fresnel-Kirchhoff diffraction theory, which is the basis for the correction of probe sample volume and particle size. The CPI is able to sample particles within the size range of approximately 10 to 2000 microns. Sampling efficiency decreases as particle size decreases from 20 microns as a threshold shadow depth is required for detection. The depth of field of the particle is constrained so that the images are not in poor focus.The limitations of the probe are discussed in Connolly et al. (2005). Image processing techniques are applied to the particle images, so that particles can be sized, and classified into droplets, or numerous ice particle habits. When particle size increases above 400 μm, the sampling efficiency drops off gradually due to the fact that the overlapping cross section of particles with the sample area decreases.

The Welas particle probe uses white light scattering collected at 90±12° scattering angle from a sample volume defined by an apertured light source to measure particles in the size range 0.8 to 46 μm (for water droplets). The flow speed used for this instrument was 5 l min^{-1}.

5 Results

5.1 Time series

We present four time series to demonstrate the ice nucleation behavior of the dust samples at different temperatures. Three examples result from using the Asian dust sample and one from the Saharan dust sample. The features of the ice nucleation that we will highlight using either the Asian or Saharan sample are seen for both of these

dust samples at the same temperature.

Each time series figure comprises of 6 panels showing 1-s data as a function of time since the start of pumping. Panel (a) shows the pressure forcing and temperature change imposed in the AIDA cloud chamber. Panel (b) gives the saturation ratio with respect to water and ice throughout the experiment. Panel (c) is a plot of the SID asphericity parameter, Af, each point represents a single particle measurement. In panel (d) various concentrations are depicted (5-s smoothing): The total SID concentration, the concentration of SID particles with $Af>12$ (non-spherical particles), the concentration of SID particles with "spherical size" $>3\,\mu$m and the CPI concentration. Panel (e) shows single particle measurements of SID particle "spherical size" and a contour plot of the CPI size distribution to provide the reader with a qualitative indication of when larger ice particles are present. Finally, panel (f) shows the activated fraction of ice particles defined by the concentration of particles with 10-s binned $Af>12$ compared to the instantaneous aerosol concentration defined by the (initial aerosol concentration × pressure)/(initial pressure). Running vertically throughout the figure are dotted lines that indicate when the fraction activated nominally exceeds 0.5% and 8%. Ice concentrations were determined by the SID concentration of non-spherical particles ($Af>12$). Because the determination of particle sphericity can lead some particles to be classified as spherical, the concentration of ice crystals using this criteria will be underestimated. By comparing the activated fraction derived from using shape and size towards the end of each experiment when the humidity is below water saturation but saturated with respect to ice and by intercomparison with other optical particle counters we find that the using the $Af>12$ criteria the activated fraction is underestimated by a factor of 1.6 compared to the fraction greater than $3\,\mu$m. Consequently we have multiplied the $Af>12$ activated fraction by 1.4 and this is shown in panel (f). We also note here that there may be some time delay between ice particles nucleating and their subsequent detection with SID. Möhler et al. (2005) have attempted to estimate this delay by invoking a simple growth model. Such an approach is more difficult to apply when we are considering the shape as well as the size of the particles and may not be necessary

at the relatively warm temperatures considered here: Möhler et al. (2005) estimate a delay of 4 s for the growth to ∼1 μm at −50°C, the coldest temperatures presented in this paper. Nevertheless, this difference in approach to estimating the onset of nucleation leads to slight differences in conditions at which the nucleation is observed, but still within the estimated experimental errors. Various parameters relating to the ice nucleation events are given in Table 1. Example CPI imagery from these experiments can be seen in Fig. 5.

Figure 1 shows one example from the coldest series of ice nucleation events sampled with the SID probe. Run 29 (AD1) starts at −51°C and is cooled to −57°C over ∼400 s. Around 0s the background aerosol that can be detected by SID can be seen in panel (e). This aerosol generally has a "spherical size" <3 μm for all of the experiments and we use this as a threshold size between activated particles and aerosol. At 50 s panel (e) shows a rapid increase in the size of particles, panel (d) indicates increases in SID concentrations and panel (c) shows the abrupt appearance of particles with Af values greater than 12. At 250 s there is another burst of ice particle production visible in panel (e) as a second branch of increasing SID particle size. This is accompanied by a step increase in SID concentrations shown in panel (d). The particle concentrations then remain fairly constant until the humidity falls below ice saturation. The two ice nucleation events occur at supersaturation with respect to ice of 10% and 50% and activate ∼5% and ∼30% of the aerosol, respectively. CPI imagery for this experiment in Fig. 5 shows rosette-like habits.

Figure 2 is for run 24 (AD1) which began at −36°C and cooled to −44°C after 270 s. As in the previous case it is possible to discern two ice nucleation events. One occurs at 70 s marked by the growth of a few ice particles in panel (e) and then a more obvious second event at 150 s that is close to water saturation (∼95%). Variability of the humidity and temperature fields within the chamber could result in regions at water saturation. If so, then any droplets produced were either not sampled by the SID or smaller than ∼3 μm in diameter This figure exemplifies the difficulties in determining the onset of ice nucleation. The CPI concentration in panel (d) supports the sugges-

tion that there is a nucleation event before the one at 150 s, identified by the growth of particles measured by SID. As in the previous example the activated fraction of aerosol from the primary and secondary nucleation events is ∼5% and ∼30%. CPI imagery for this experiment in Fig. 5 again shows rosette-like habits.

Figure 3 is from run 20 (AD1) and appears different to the previous two examples. The run began at −23°C and was cooled to −32°C over 110 s. In this case it can be seen that at 100 s there is a rapid production of large numbers of particles (panel d). Referring to the asphericity parameter in panel (c) suggests that from 100 s to 150 s the cloud is dominated by water droplets (asphericity values <12). Looking at the concentration of non-spherical particles and CPI concentration (panel d) as well as the particle sizes (panel e) indicates that ice particles were present almost coincidently with the formation of droplets, but not before. This suggests that the dominant ice nucleation mode in this case is an immersion or condensation mechanism and activated about 10% of the aerosol (panel f). Again, CPI imagery for this experiment in Fig. 5 shows rosette-like habits, although the coldest temperature attained during this experiment was only −32°C, therefore they may be some other type of polycrystal habit. Although it should be noted that habit discrimination using the CPI is difficult for particles of this size.

Figure 4 results from run 31 which is part of the series of warmest runs presented here and uses the Saharan dust sample (SD2). In this case the cooling is from −19°C to −26°C in 280 s. Panel (e) shows the growth of particles starting at 40 s into the run. Panel (c) suggests that water droplets are present throughout the run until 470 s. One unusual aspect of this series of runs is that the droplet concentration shows a peak near the beginning of the run and then falls to a plateau later. Comparison with the Welas instrument (Möhler et al., 2005) suggests that the SID is not seeing a large fraction of the water droplets. One suggestion for this discrepancy is that some water droplets are evapourating at these warm temperatures as they travel down the SID sample tube from the AIDA chamber. Nevertheless, we still observe that ice is formed at the same time as the droplets. Evidence for this comes from the CPI imagery which shows low

ACPD
6, 1509–1537, 2006

EGU

concentrations of ice particles. In this series of experiments (30, 31, 32), the aerosol concentrations were not available. Instead we used the peak droplet concentration from the Welas probe as experiments 18–21 showed that all of the aerosol became activated under the forcing conditions applied. CPI imagery in Fig. 5 for this experiment appears to show the coexistence of large droplets with irregular shaped ice crystals. A high resolution image of the particle shown in the 480–600 s 52–87 μm panel suggests that this is a two crystal aggregate.

5.2 Synthesis

As mentioned above we have identified when the activated fraction of aerosol exceeded 0.5% and 8%. In practice, it was found that this choice of thresholds readily located the beginning of both the first and second nucleation event when two events were obvious. The results of this analysis are shown in Figs. 6 and 7. Figure 6 indicates the relative humidity and temperature associated with the points exceeding the 0.5% and 8% ice fraction thresholds. Three regions have been identified on the plot. In region I droplets were observed to form at the same time or prior to the formation of ice. Region II contains the primary nucleation events and region III contains the secondary events. Figure 7 shows the maximum fraction activated as a function of the temperature at which 0.5% were first activated.

6 Discussion

The experimental results can be divided into nucleation behavior at temperatures warmer and colder than −40°C. For temperatures warmer than −40°C denoted by region I in Fig. 6, the onset of ice nucleation activating aerosol fractions greater than 0.5% is coincident with the production of water droplets as the chamber reaches water saturation. Thus nucleation occurring in region I is via an immersion, condensation mode or homogeneous freezing for the experiments near −40°C. Roberts and Hal-

lett (1968) also observed, using a static diffusion chamber, that mineral dust samples warmer than a critical temperature needed to be brought to water saturation before ice formed. However, in their study, the coldest temperature for which this behavior was observed was −28°C. The maximum activated fraction during the experiment for the region I nucleation events (Fig. 7) climbs by roughly a factor of 10 from 5 to 50% from −20 to −40°C, respectively. The high fractions seen for experiments 35–37 may result from additional ice forming via homogeneous nucleation at around −40°C.

For temperatures colder than −40°C Fig. 1 indicated that dual nucleation events were observed where ice formed at two distinct ice saturation ratios with a hiatus clearly visible in the experiments where the pumping speed was slow enough to provide a low cooling rate. This behavior was observed for both the Asian and Saharan desert dust samples. In Fig. 6, region II represents the primary activation during these experiments and region III marks the secondary nucleation event. In each of these series of experiments (22–25, 26–29, 40–42), the first expansion did not show a clear dual nucleation signature. However, the >0.5% and >8% activations for 22, 26, 40 appear to cluster well with the results from the later experiments in each series. This suggests that if the first runs are carried out at slower pumping speeds then the dual nucleation will become apparent for the first expansion also – not because cooling rate is expected to affect the cooling rate (Möhler et al., 2005), but simply because this allows a longer temporal seperation between the nucleation events.

The activation of >0.5% of the aerosol occurs at an ice saturation ratio of 1.1 to 1.3. Archuleta et al. (2005) find that 1% of 200 nm asian mineral dust activates with a ice saturation ratio of ∼1.35. For the dust samples used here the mode in the particle size is approximately twice as large and bigger particles were also contained in the sample tested (see Sect. 3). The maximum activated fraction of desert dust following the secondary nucleation event appears constant and in the 20–40% range. The primary nucleation mode typically activated <5% of the aerosol sample before the effects of the secondary mode became important. The ice saturation ratio at which the region II ice nucleation events occurred points to deposition nucleation as the likely formation

mechanism. The situation is not so clear for the secondary mode which activates >8% of the aerosol sample at ice saturation ratios between 1.35 and 1.5. These saturation ratios are close to what Zuberi et al. (2002) obtained for dust samples immersed in aqueous droplets ($(NH_4)_2SO_4$-H_2O, 10–50 μm in size). In this case, no droplets were observed, but Archuleta et al. (2005) suggest that condensation on hydrophillic sites may be important at these temperatures and humidities. Therefore, it is unclear whether the secondary nucleation events (region III) represent a further deposition nucleation mode, or a condensation freezing mode facilitated by the presence of some soluble material on the surface of the aerosol. Future experiments should aim to analyse the ice crystal residuals in order to test these assertions.

The deposition nucleation (region II, activated fraction >0.5%) is only observed at temperatures colder than −40°C and absent from the experiments performed at temperatures warmer than −40°C. This is puzzling as supersaturations with respect to ice of in excess of 20% are attained before the droplets are activated at these warmer temperatures. One possible reason for this difference is that the nucleation rate falls well below a threshold required for the production of sufficient ice crystals to be detected in this experimental setup. Other laboratory experiments using pure minerals (Roberts and Hallett, 1968; Bailey and Hallett, 2002) have shown that deposition nucleation readily occurred at temperatures warmer than −40°C. This difference may be compositional, size related or a result of the SID detection thresholds. The SID samples approximately 1 cm^3 per second and the results are accumulated over 10s for estimating the activated fraction. This sets a realistic detection limit of ~0.5 cm^{-3}. In future experiments we will use higher sampling rates to try and resolve this apparent discrepancy.

Roberts and Hallett (1968) also reported that pre-activation of aerosol leads to ice production at lower saturation ratios. We are unable to comment on this – from examination of the starting aerosol concentration (Table 1) it is likely that all of the ice and hence ice nuclei sediment out during the course of each experiment.

The dual nucleation behavior presented in Figs. 1 and 2 and evident in many of the

experiments performed means that it is difficult to simply assign a bulk mineral dust sample with a nucleation rate. As Archuleta et al. (2005) show, there is at least a size dependence that needs to be taken into account. For this study it is possible that broadness of the size distribution of aerosol used contributes to the presence of the dual nucleation behavior, but it is also possible that mineralogically or chemically or diverse subsets of particles are included in the dust samples tested here. Future work needs to include the capture and analysis of ice crystal residuals that form at different saturation ratios.

7 Conclusions

Two desert dust samples (modal diameter 300–500 nm) from the Sahara and Asia were used in ice nucleation experiments between −20°C and −60°C in the AIDA cloud chamber. Very similar behaviour was observed for both dust samples. We observed dual nucleation events during single expansions at temperatures colder than −40°C. The primary nucleation event is likely to be deposition nucleation, but the secondary event is either a further deposition mode exhibited by particles of different sizes or mineralogical/chemical composition or a condensation mode facilitated by the presence of soluble material on the desert dust. At temperatures warmer than −40°C droplets were formed before and at the same time as ice crystals were formed, presumably via and immersion or condensation ice nucleation mode and no deposition mode was observed. The maximum activated fraction of the desert dust sample forming ice varied from ∼5–10% at −20°C to 20–40% at temperatures colder than −40°C.

Acknowledgements. We gratefully acknowledge the support of AIDA staff members R. Buschbacher, T. Chudy, E. Kranz, G. Scheurig and S. Vogt for support during the campaigns. We thank L. Schutz (Univ. Mainz, Germany) for supplying the Asian dust sample, K. Megahed for supplying the Saharan dust samples and C. Adelhelm (IMF I, Forschungszentrum Karlsruhe) for XRF analysis of the mineral dust samples. We also thank E. Hirst (Univ. Hertfordshire, England) for making modifications to SID to allow its use at AIDA.

References

Archuleta, C. M., DeMott, P. J., and Kreidenweis, S. M.: Ice nucleation by surrogates for atmospheric mineral dust/sulfate particles at cirrus temperatures, Atmos. Chem. Phys., 5, 3391–3436, 2005.

Bailey, M. and Hallett, J.: Nucleation effects on the habit of vapour grown ice crystals from −18 to −42 degrees C, Quart. J. Royal Met. Soc., 128, 1461–1483, 2002.

Cziczo, D. J., Murphy, D. M., Hudson, P. K., and Thomson, D. S.: Single particle measurements of the chemical composition of cirrus ice residue during CRYSTAL-FACE, J. Geophys. Res., 109(D4), art. no. D04201, doi:10.1029/2003JD003942, 2004.

DeMott, P. J., Sassen, K., Poellot, M. R., Baumgardner, D., Rogers, D. C., Brooks, S. D., Prenni, A. J., and Kreidenweis, S. M.: African dust aerosols as atmospheric ice nuclei, Geophys. Res. Lett., 30(14), art. no. 1732, doi:10.1029/2003GL017410, 2003.

Field, P. R., Cotton, R. J., Noone, K., et al.: Ice nucleation in orographic wave clouds: Measurements made during INTACC, Quart. J. Royal Met. Soc., 127, 1493–1512, 2001.

Field, P. R., Hogan, R. J., Brown, P. R. A., Illingworth, A. J., Choularton, T. W., Kaye, P. H., Hirst, E., and Greenaway, R.: Simultaneous radar and aircraft observations of mixed-phase cloud at the 100 m scale, Quart. J. Royal Met. Soc., 130, 1877–1904, 2004.

Hirst, E., Kaye, P. H., Greenaway, R. S., Field, P., and Johnson, D. W.: Discrimination of micrometre-sized ice and super-cooled droplets in mixed-phase cloud, Atmos. Env., 35, 33–47, 2001.

Hung, H.-M., Malinowski, A., and Martin, S. T.: Kinetics of heterogeneous ice nucleation on the surfaces of mineral dust cores inserted into aqueous ammonium sulfate particles, J. Phys. Chem. A., 107, 1296–1306, 2003.

Isono, K., Komabayasi, M., and Ono, A.: The nature and origin of ice nuclei in the atmosphere, J. Meteor. Soc. Japan, 37, 211–233, 1959.

Jensen, E., Starr, D., and Toon, O. B.: Mission investigates tropical cirrus clouds, EOS, 85, 45–50, 2004.

Möhler, O., Stetzer, O., Schaefers, S., Linke, C., Schnaiter, M., Tiede, R., Saathoff, H., Kramer, M., Mangold, A., Budz, P., Zink, P., Schreiner, J., Mauersberger, K., Haag, W., Karcher, B., and Schurath, U.: Experimental investigation of homogeneous freezing of sulphuric acid particles in the aerosol chamber AIDA, Atmos. Chem. Phys., 3, 211–223, 2003.

Möhler, O., Field, P., Connolly, P., Saathoff, H., Schnaiter, M., Wagner, R., Cotton, R., Krämer,

M., Mangold, A., and Heymsfield, A.: Efficiency of the deposition mode of ice nucleation on mineral dust particles, Atmos. Chem. Phys. Discuss., 6, 1539–1577, 2006.

Roberts, P. and Hallett, J.: A laboratory study of the ice nucleating properties of some mineral particulates, Quart. J. Royal Met. Soc., 94, 25–34, 1968.

Sassen, K., DeMott, P. J., Prospero, J. M., and Poellot, M. R.: Saharan dust storms and indirect aerosol effects on clouds: CRYSTAL-FACE results, Geophys. Res. Lett., 30(12), art. no. 1633, doi:10.1029/2003GL017371, 2003.

Targino, A. C., Krejci, R., Noone, K. J., and Glantz, P.: Single particle analysis of ice crystal residuals observed in orographic wave clouds over Scandinavia during INTACC experiment, Atmos. Chem. Phys. Discuss., 5, 8055–8090, 2005.

Zuberi, B., Bertram, A. K., Cassa, C. A., Molina, L. T., and Molina, M. J.: Heterogeneous nucleation of ice in (NH4)(2)SO4-H2O particles with mineral dust immersions, Geophys. Res. Lett., 29(10), art. no. 1504, doi:10.1029/2001GL014289, 2002.

Table 1. Ice nucleation exceeding active fraction thresholds of 0.5 and 8%.

Exp	Temperature	>0.5% Pressure	Saturation Ratio	Temperature	>8% Pressure	Saturation Ratio	Max. act. Fraction	Initial aerosol Concentration	Sample
	C	mb		C	mb			cm^{-3}	
18	−29.4	829	1.30	0.0	0	0.00	0.09	215	AD1
19	−30.2	844	1.31	−31.4	806	1.31	0.14	152	AD1
20	−32.0	846	1.36	−31.8	836	1.28	0.11	105	AD1
21	−33.4	856	1.38	−33.5	838	1.32	0.11	75	AD1
22	−40.5	900	1.30	−42.2	845	1.38	0.15	139	AD1
23	−41.2	892	1.30	−42.6	839	1.42	0.17	94	AD1
24	−41.3	892	1.27	−42.7	855	1.39	0.33	68	AD1
25	−40.4	901	1.12	–	–	–	0.06	45	AD1
26	−52.7	972	1.17	−53.9	950	1.31	0.28	119	AD1
27	−53.4	958	1.22	−55.0	924	1.43	0.30	72	AD1
28	−53.0	963	1.14	−55.7	893	1.46	0.19	44	AD1
29	−53.2	953	1.14	−55.9	875	1.48	0.33	29	SD2
30	−21.6	951	1.22	–	–	–	0.06	353	SD2
31	−21.1	952	1.20	–	–	–	0.03	150	SD2
32	−19.7	973	1.03	–	–	–	0.08	24	SD2
35	−38.0	928	1.43	−38.3	921	1.46	0.20	153	SD2
36	−38.5	923	1.42	−38.8	915	1.41	0.45	88	SD2
37	−36.1	963	1.15	−38.7	907	1.42	0.69	38	SD2
40	−51.7	945	1.25	−53.1	917	1.41	0.20	107	SD2
41	−52.0	941	1.26	−53.6	899	1.46	0.21	64	SD2
42	−51.5	955	1.17	−53.9	895	1.50	0.36	39	SD2

ACPD
6, 1509–1537, 2006

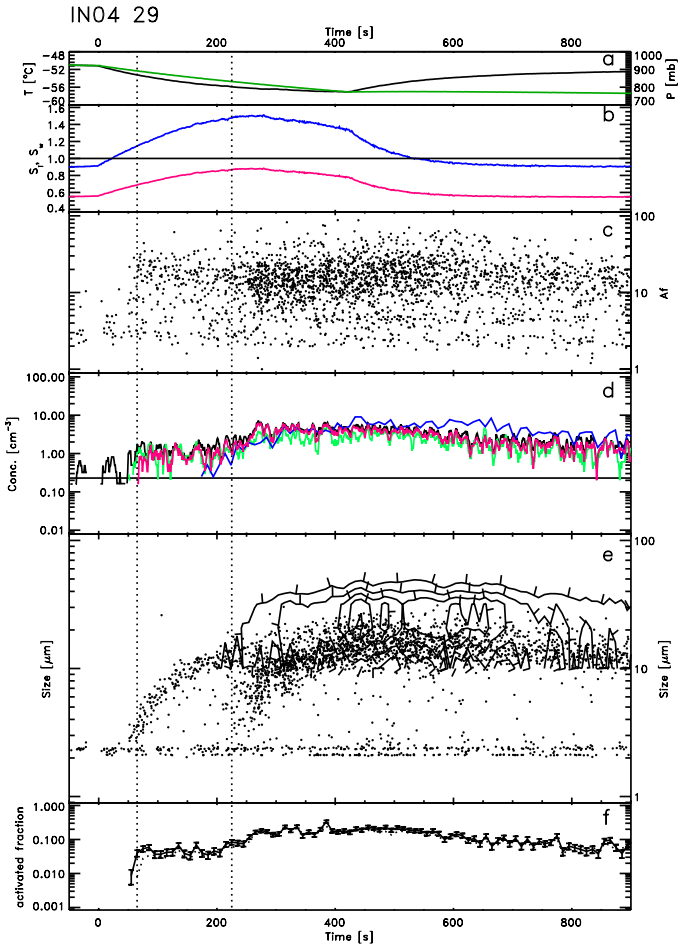
IN04 29
Time [s]
T [°C]
P [mb]
a
b
S_i, S_w
c
Af
d
Conc. [cm^{-3}]
e
Size [μm]
f
activated fraction
Time [s]

Fig. 1.

Fig. 1. Experiment IN04 29. Panel **(a)** shows the pressure forcing (green) and temperature change imposed in the AIDA cloud chamber (black). Panel **(b)** gives the saturation ratio with respect to water (red) and ice (blue) throughout the experiment. Panel **(c)** is a plot of the SID asphericity parameter, Af, each point represents a single particle measurement. In panel **(d)** various concentrations are depicted (5-s smoothing): The total SID concentration (black), the concentration of SID particles with $Af>12$ (non-spherical particles, green), the concentration of SID particles with "spherical size" $>3\,\mu$m (red) and the CPI concentration (blue). Panel **(e)** shows single particle measurements of SID particle "spherical size" and a contour plot of the CPI size distribution (tickmarks indicate "downhill" direction). Panel **(f)** shows 10-s values of the activated fraction of desert dust (see text). Poisson counting errors are also shown. The solid line is the derived from particle concentrations for which $Af>12$ (corrected, see text) and the dotted line is the for particles with sizes greater than $3\,\mu$m.

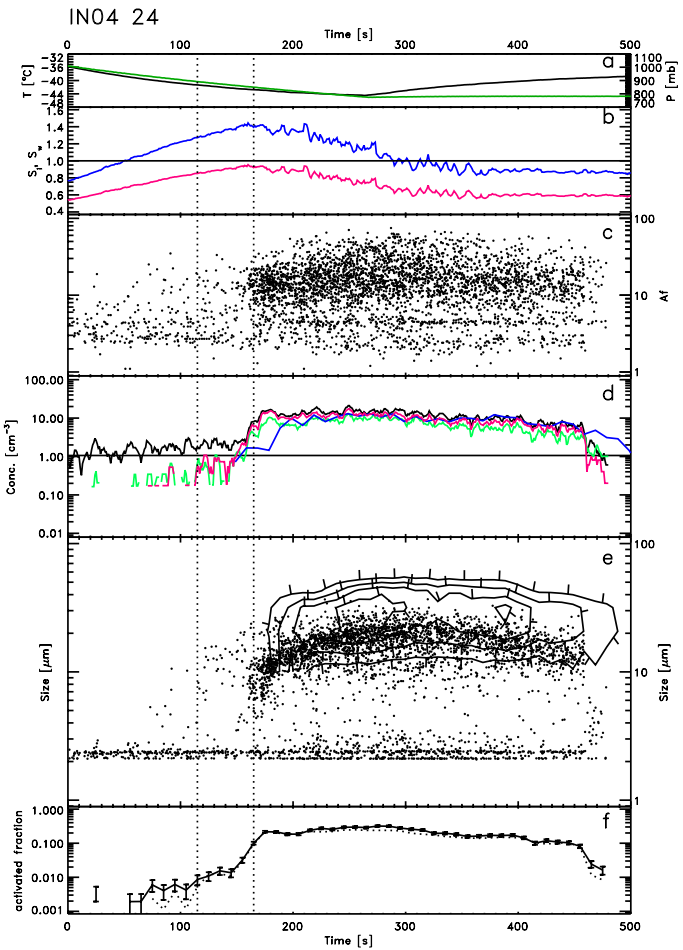
IN04 24
Time [s]
T [°C]
P [mb]
a
b
S_i, S_w
c
Af
d
Conc. [cm^{-3}]
e
Size [μm]
f
activated fraction
Time [s]

Fig. 2.

Fig. 2. Experiment IN04 24. Panel **(a)** shows the pressure forcing (green) and temperature change imposed in the AIDA cloud chamber (black). Panel **(b)** gives the saturation ratio with respect to water (red) and ice (blue) throughout the experiment. Panel **(c)** is a plot of the SID asphericity parameter, Af, each point represents a single particle measurement. In panel **(d)** various concentrations are depicted (5-s smoothing): The total SID concentration (black), the concentration of SID particles with $Af>12$ (non-spherical particles, green), the concentration of SID particles with "spherical size" $>3\,\mu$m (red) and the CPI concentration (blue). Panel **(e)** shows single particle measurements of SID particle "spherical size" and a contour plot of the CPI size distribution (tickmarks indicate "downhill" direction). Panel **(f)** shows 10-s values of the activated fraction of desert dust (see text). Poisson counting errors are also shown. The solid line is the derived from particle concentrations for which $Af>12$ (corrected, see text) and the dotted line is the for particles with sizes greater than $3\,\mu$m.

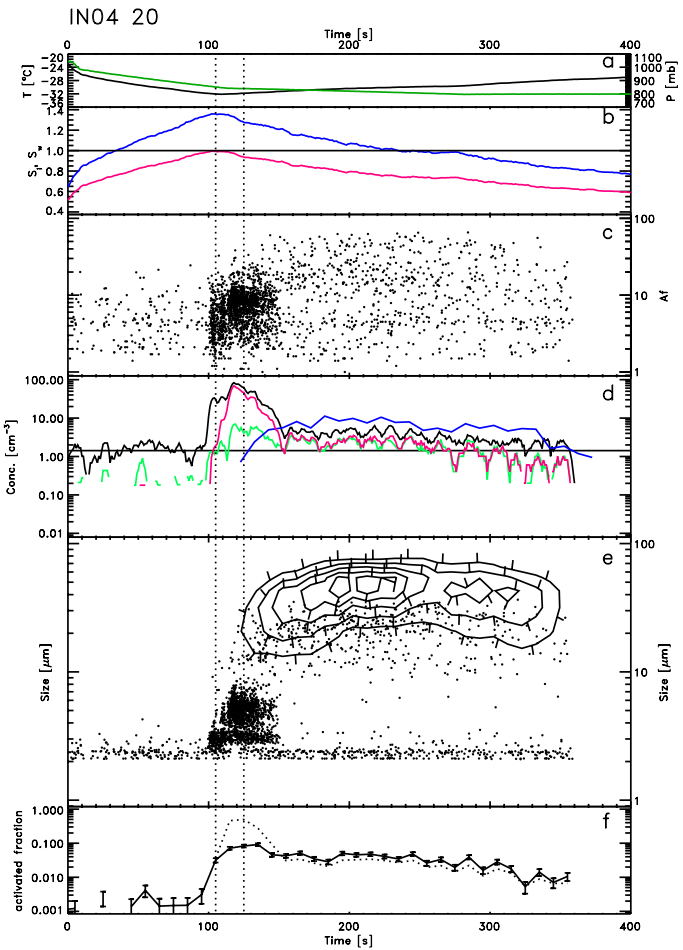
IN04 20
Time [s]
T [°C]
P [mb]
a
b
S_i, S_w
c
Af
d
Conc. [cm^{-3}]
e
Size [μm]
f
activated fraction
Time [s]

Fig. 3.

Fig. 3. Experiment IN04 20. Panel **(a)** shows the pressure forcing (green) and temperature change imposed in the AIDA cloud chamber (black). Panel **(b)** gives the saturation ratio with respect to water (red) and ice (blue) throughout the experiment. Panel **(c)** is a plot of the SID asphericity parameter, Af, each point represents a single particle measurement. In panel **(d)** various concentrations are depicted (5-s smoothing): The total SID concentration (black), the concentration of SID particles with $Af>12$ (non-spherical particles, green), the concentration of SID particles with "spherical size" $>3\,\mu$m (red) and the CPI concentration (blue). Panel **(e)** shows single particle measurements of SID particle "spherical size" and a contour plot of the CPI size distribution (tickmarks indicate "downhill" direction). Panel **(f)** shows 10-s values of the activated fraction of desert dust (see text). Poisson counting errors are also shown. The solid line is the derived from particle concentrations for which $Af>12$ (corrected, see text) and the dotted line is the for particles with sizes greater than $3\,\mu$m.

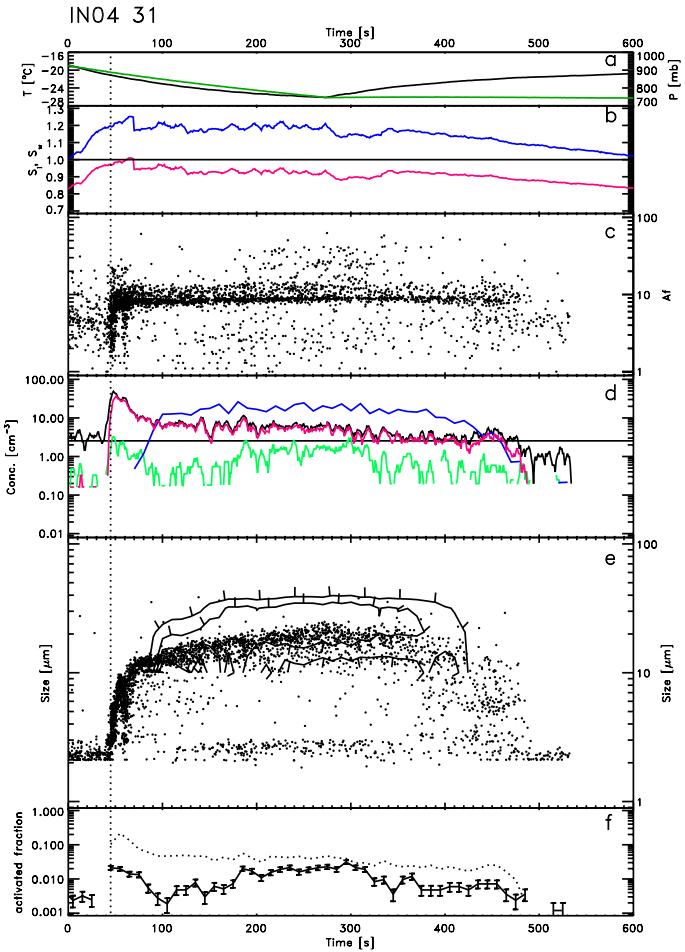
IN04 31
Time [s]
T [°c]
P [mb]
a
b
S_i, S_w
c
Af
d
Conc. [cm⁻³]
e
Size [μm]
f
activated fraction
Time [s]

Fig. 4.

Fig. 4. Experiment IN04 31. Panel **(a)** shows the pressure forcing (green) and temperature change imposed in the AIDA cloud chamber (black). Panel **(b)** gives the saturation ratio with respect to water (red) and ice (blue) throughout the experiment. Panel **(c)** is a plot of the SID asphericity parameter, Af, each point represents a single particle measurement. In panel **(d)** various concentrations are depicted (5-s smoothing): The total SID concentration (black), the concentration of SID particles with $Af>12$ (non-spherical particles, green), the concentration of SID particles with "spherical size" $>3\,\mu$m (red) and the CPI concentration (blue). Panel **(e)** shows single particle measurements of SID particle "spherical size" and a contour plot of the CPI size distribution (tickmarks indicate "downhill" direction). Panel **(f)** shows 10-s values of the activated fraction of desert dust (see text). Poisson counting errors are also shown. The solid line is the derived from particle concentrations for which $Af>12$ (corrected, see text) and the dotted line is the for particles with sizes greater than $3\,\mu$m.

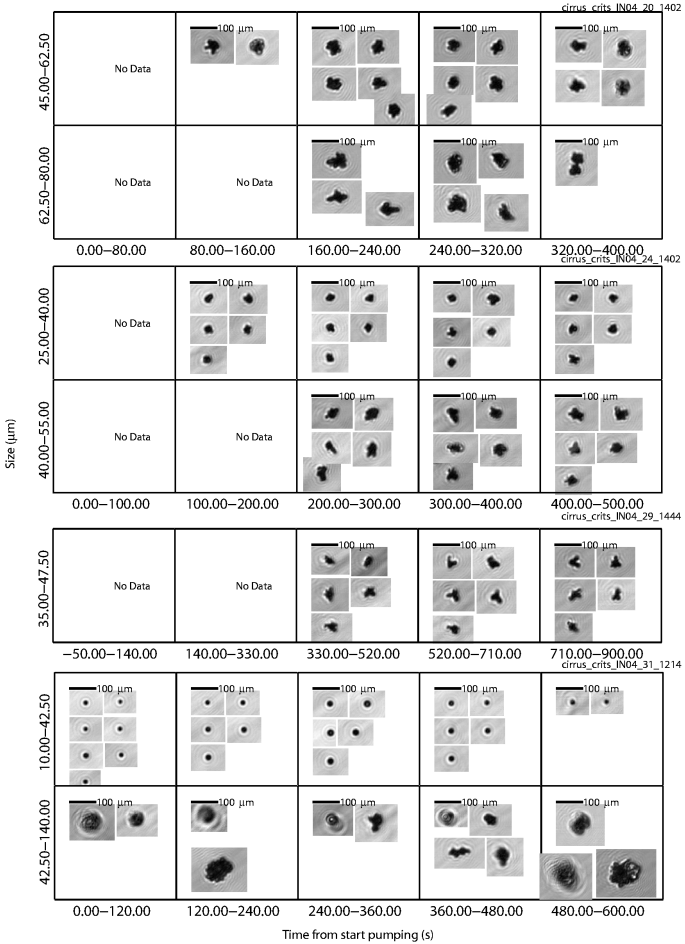

Fig. 5. Example CPI imagery from the four experiments shown in Figs. 1–4. The x-axis represents time since pumping started and the values on the y-axis indicate the size range of particles considered.

ACPD
6, 1509–1537, 2006

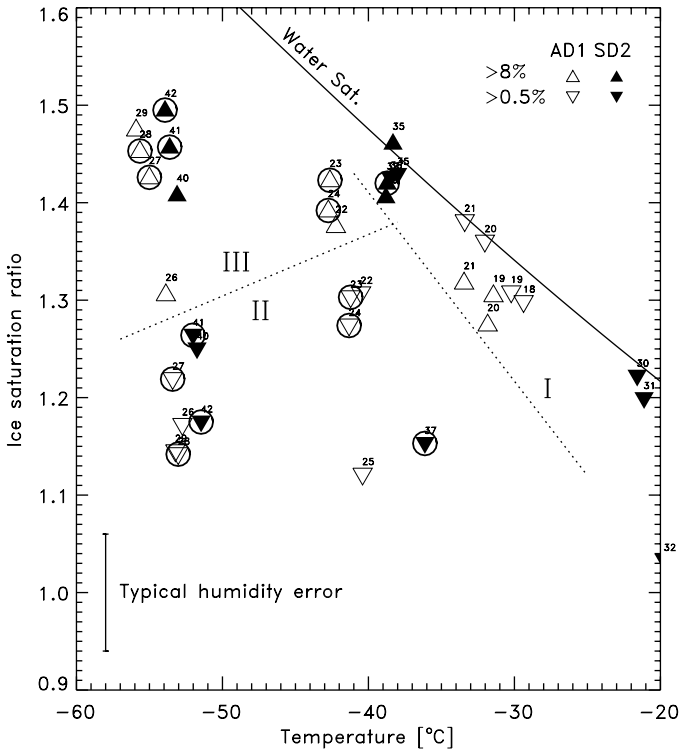

Fig. 6. Plot shows the ice saturation ratio and temperature at which ice nucleation was observed to begin. Open symbols are the results for the Asian desert dust sample (AD1), filled symbols are for the Saharan desert dust sample (SD2). The numbers adjacent to each symbol represent the experiment number (see Table 1). Downward pointing triangles denote when the fraction of aerosol forming ice crystals exceeded 0.5%. Upward pointing triangles denote when the fraction of aerosol forming ice crystals exceeded 8%. Circled symbols indicate when examination of the time series for the experiment clearly showed two distinct nucleation events.

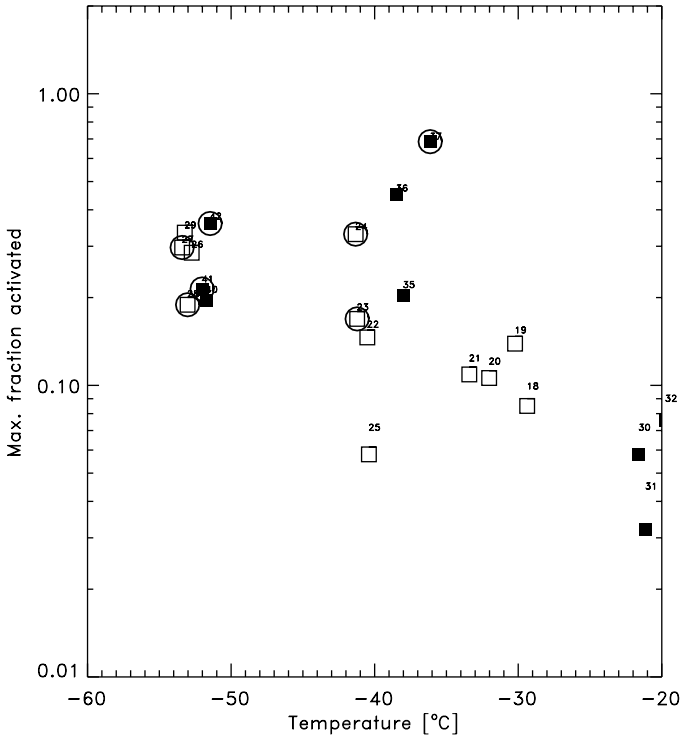

Fig. 7. This plot shows the maximum fraction of aerosol (10-s) activated to form ice as a function of temperature when the fraction exceeded 0.5%. Open symbols are the results for the Asian desert dust sample (AD1), filled symbols are for the Saharan desert dust sample (SD2). The numbers adjacent to each symbol represent the experiment number (see Table 1). Circles represent experiments where only a single nucleation event was observed. The triangles and squares represent experiments where two nucleation modes were observed during a single experiment.The dotted line nominally divides the nucleation events into immersion and deposition modes (see text). Circled symbols indicate when examination of the time series for the experiment clearly showed two distinct nucleation events.